Annals of Pharmacy Practice and Pharmacotherapy
ISSN: 3062-4436
2023, Volume 3, Page No: 228-242

Available online at: www.galaxypub.co/page/journals

Galaxy Publication

Engineered Nanogels Incorporating Gold Nanorods for Cascade-Enhanced Photothermal–Enzymatic Synergistic Therapy

Jonathan P. Reed[1], Steven H. Young[1]*

[1]Department of Clinical Pharmacy, School of Pharmacy, University of Washington, Seattle, United States.

***E-mail** ✉ s.h.young_uw@outlook.com

Received: 15 August 2023; **Revised:** 19 November 2023; **Accepted:** 21 November 2023

ABSTRACT

Cancer therapies based on reactive oxygen species (ROS) show great potential by disrupting the redox equilibrium in tumor cells through multiple pathways. In particular, approaches that combine physical and biochemical activation have gained attention due to their precise spatiotemporal control, minimal toxicity, and high treatment efficiency. In this study, we developed a nanogel complex that functions as a multilevel ROS-amplifying system by incorporating chloroperoxidase (CPO) into gold nanorod-based nanogels (ANGs) for cascade-enhanced photothermal-enzymatic tumor therapy. Upon near-infrared (NIR) laser irradiation, the AuNR nanogels induced local hyperthermia, which amplified exogenous ROS (including H2O2) via cellular stress responses. This effect enhanced the enzyme-mediated reaction of the encapsulated CPO with the abundant endogenous H2O2 in tumor cells, significantly raising intracellular ROS to levels sufficient for improved therapeutic efficacy. Both in vitro and in vivo experiments confirmed the cascade-amplified ROS-driven antitumor activity, highlighting a promising multimodal synergistic strategy for cancer treatment.

Keywords: Nanogels, Photothermal-enzymatic synergistic therapy, ROS-based nanodynamic therapies, Gold nanorods

How to Cite This Article: Reed JP, Young SH. Engineered Nanogels Incorporating Gold Nanorods for Cascade-Enhanced Photothermal–Enzymatic Synergistic Therapy. Ann Pharm Pract Pharmacother. 2023;3:228-42. https://doi.org/10.51847/sHukOXos7w

Introduction

Cancer poses a significant risk to human health and survival due to its heterogeneous and intricate nature. Therapeutic strategies tailored to cancer typically rely on the established hallmarks of the disease [1]. Reactive oxygen species (ROS) are recognized as key signaling entities that influence cancer cells, contributing to the development of diverse cancer hallmarks across all phases of tumor progression [2]. ROS encompass highly reactive molecules such as superoxide anions ($O_2^{\cdot -}$), hydroxyl radicals (·OH), singlet oxygen ($^1O_2$), and hydrogen peroxide (H_2O_2), which drive numerous oxidative processes in biology and are essential for normal physiological activities [3, 4]. In healthy cells, ROS production and scavenging are precisely regulated through antioxidant mechanisms to maintain equilibrium [5]. Cancer cells, however, exhibit higher baseline ROS levels and greater dependence on antioxidant pathways, rendering them more vulnerable to further ROS accumulation than normal cells [6, 7]. Excessive ROS can overwhelm antioxidant capacities, leading to increased oxidative stress and irreversible harm to DNA, proteins, and lipids, ultimately triggering cell death [8]. Therefore, selectively increasing ROS concentrations beyond the cellular tolerance limit specifically within tumor sites represents a clever and effective approach for cancer therapy, sparing healthy tissues from significant harm [9, 10].

Considerable research has led to the development of multiple ROS-based methods aimed at disturbing tumor redox balance for therapeutic purposes [11-13]. For example, photodynamic therapy (PDT) and sonodynamic therapy (SDT) serve as representative techniques for producing external ROS, where photosensitizers or sonosensitizers are activated by light or ultrasound to transform molecular oxygen (O_2) into highly toxic $^1O_2$ [14-20]. Chemodynamic therapy (CDT), a more recent approach, utilizes inorganic nanoparticles to catalyze Fenton

or Fenton-like reactions, efficiently converting intrinsic H_2O_2 into deadly ·OH radicals within tumors [21-23]. Notably, drawing from the neutrophil's immune response involving myeloperoxidase-catalyzed reactions with H_2O_2, a sustained enzymatic ROS elevation strategy has emerged, known as enzyme dynamic therapy (EDT) [24], [25, 26]. EDT involves the biocatalytic transformation of intrinsic ROS precursors (H_2O_2 and $O_2{\cdot}^-$) into potent $^1O_2$, profoundly disrupting cellular redox equilibrium and promoting tumor cell apoptosis or necrosis. Nevertheless, relying solely on one biocatalytic modality in ROS-based treatments often yields suboptimal results due to constraints related to limited endogenous H_2O_2 availability and the complex adaptive redox systems in cancer cells. Consequently, combining EDT with additional therapeutic approaches to create amplified cascade effects is highly sought after.

Photothermal therapy (PTT) employs photothermal converters to transform near-infrared (NIR) light into heat for direct tumor destruction and has emerged as an appealing cancer treatment option [27-31]. PTT attracts substantial interest because of its non-invasive nature, precise control over timing and location, and ability to penetrate deeper tissues [32]. Research indicates that elevated temperatures not only cause cancer cell death but also stimulate ROS production (such as H_2O_2 or $O_2{\cdot}^-$) via cellular stress responses, paving the way for combined PTT/EDT to sequentially boost ROS and surpass antioxidant thresholds [33, 34]. Additionally, PTT operates without relying on oxygen, offering a clear advantage over other stimulus-dependent therapies that may be ineffective in low-oxygen tumor environments [35]. Overall, enhancing ROS through the combination of external PTT and internal EDT provides a practical avenue for better tumor control at specific sites.

In this work, inspired by the light-triggered heating capability of PTT and the robust catalytic efficiency of EDT, we designed a hybrid nanogel platform encapsulating chloroperoxidase (CPO) within gold nanorod (AuNR)-containing nanogels (ANGs) for sequential enhancement of photothermal-enzymatic treatment in aggressive cancers. AuNRs provide excellent photothermal performance, allowing precise control over external ROS generation under NIR exposure while boosting H_2O_2 levels [36, 37]. CPO facilitates the enzymatic reaction of elevated endogenous H_2O_2 with halide ions to produce harmful $^1O_2$ inside tumor cells [38], thereby further raising ROS concentrations. This stepwise ROS escalation strategy cooperatively pushes intracellular ROS past critical limits, facilitating cancer cell death. As a result, this nanogel construct offers a potential multimodal platform for targeted, sequential amplification of oxidative damage via concurrent external and internal ROS elevation to enhance anticancer efficacy.

Materials and Methods

All reagents were utilized directly without additional purification. $NaBH_4$, $AgNO_3$, and H_2O_2 were sourced from Sinopharm Chemical Reagent Co., Ltd. (Shanghai, China). Chloroauric acid ($HAuCl_4$), cetyltrimethylammonium bromide (CTAB; 1.3220 g/mL), N-(3-dimethylaminopropyl)-N′-ethylcarbodiimide hydrochloride (EDC·HCl), N-hydroxysuccinimide (NHS), phosphate-buffered saline (PBS), ascorbic acid, 2-morpholinoethanesulfonic acid (MES) solution, and Tris-HCl buffer were acquired from Baoman Biotechnology Co., Ltd. (Shanghai, China). Sodium hyaluronate (molecular weight (MW) = 3000–10000) was obtained from Shandong Freda Bioeng Co., Ltd. (Jinan, China). Acid phosphatase (AP; MW = 10 kDa; enzyme commission (EC) 3.1.3.2) and chloroperoxidase (CPO; ≥3000 U/mL; EC 1.11.1.10) were supplied by Sigma-Aldrich (Shanghai, China); N-(fluorenyl-methoxycarbonyl) tyrosine phosphate (Fmoc-Tyr(H_2PO_3)-OH), 1-hydroxybenzotriazole (HOBt), dithiothreitol (DTT), and cystamine dihydrochloride were provided by GL Biochem (Shanghai) Co., Ltd. (Shanghai, China). Singlet oxygen sensor green (SOSG) and 2′, 7′-dichlorodihydrofluorescein diacetate (DCFH-DA) were purchased from Thermo Fisher Scientific Inc. (Shanghai, China). Cell Counting Kit-8 (CCK-8) was obtained from Beyotime Biotechnology (Shanghai, China). All remaining chemicals were employed as supplied without further processing.

Synthesis of gold nanorods (AuNRs)

Gold nanorods (AuNRs) were synthesized following a previously described protocol [39]. In brief, a seed solution was prepared by combining 0.25 mL of $HAuCl_4$ (0.01 M), 0.6 mL of ice-cold $NaBH_4$ (10 mM), and 7.5 mL of CTAB (0.1 M) to yield a total volume of 10 mL. The mixture was stirred for 1 min in a 30 °C water bath, during which the color shifted from colorless to brown. The solution was then maintained at 30 °C for two hours to complete seed formation. Separately, the growth solution was formulated by mixing 100 mL of CTAB (0.1 M), 3 mL of $HAuCl_4$ (0.025 M), 800 μL of $AgNO_3$ (50 mM), 2 mL of H_2SO_4, and 800 μL of ascorbic acid (0.1 M) in a

30 °C water bath; vigorous stirring rendered the initially yellow solution colorless. Finally, 0.24 mL of the seed solution was introduced into the growth solution, stirred for 1 h, and left undisturbed at 30 °C for 18 h. Excess CTAB was removed by washing the product three times with ultrapure water, followed by centrifugation (10, 000 rpm, 15 min) to isolate the AuNRs.

Preparation of thiol-modified hyaluronic acid (HA-SH) and carboxyl-modified gold nanorods (AuNRs-COOH)
HA-SH was prepared using an established procedure. First, 5 g of sodium hyaluronate (MW 3, 000–10, 000) was dissolved in 250 mL of PBS (pH 7.0). Next, 3.71 g of EDC·HCl and 5.07 g of HOBt were added, and the mixture was stirred for two hours to activate the carboxylic groups on HA. Subsequently, 8.45 g of cystamine dihydrochloride was slowly added dropwise to graft thiol functionalities. After 24 h of stirring, the product was dialyzed against deionized water for twenty fout hours using a membrane (8, 000–14, 000 Da) to eliminate unreacted reagents. Then, 9.64 g of DTT was introduced to the dialyzed solution and stirred for an additional 24 h. The mixture was further dialyzed against deionized water for 2 days to remove excess DTT. The purified HA-SH was freeze-dried and kept at −20 °C until needed.
AuNRs-COOH were obtained by dispersing the synthesized AuNRs in 15 mL of MES buffer (pH 6.7), adding lyophilized HA-SH, and stirring the suspension for 30 min at 30 °C. The resulting AuNRs-COOH were purified by three washes with MES buffer (1 M, pH 6.7) and collected via centrifugation (9, 000 rpm, fifteen minutes).

Fabrication of AuNR-containing nanogels (ANGs) and enzyme-encapsulated hybrid nanogels (ANCGs)
The prepared AuNRs-COOH were resuspended in 15 mL of MES buffer (1 M, pH 6.7). To activate surface carboxyl groups, 10 mg of EDC and 10 mg of NHS were added, followed by stirring for thirty minutes. The activated nanorods were washed three times with deionized water and then redispersed in 2 mL of acid phosphatase (AP) solution (1 mg/mL) under ultrasonication to immobilize AP onto the AuNRs. After 2 h of stirring, AP-conjugated AuNRs (AuNRs-AP) were isolated by centrifugation (9, 000 rpm) and resuspended in 30 mL of ultrapure water. Next, 30 mg of Fmoc-Tyr(H_2PO_3)-OH and 6 mg of Na_2CO_3 were added, and the mixture was stirred for 12 h at 30 °C to form the nanogel structure. The resulting ANGs were collected by centrifugation (9, 000 rpm) and rinsed three times with deionized water to eliminate residual Fmoc-Tyr(H_2PO_3)-OH.
For ANCGs preparation, the ANGs were dispersed in 2 mL of Tris-HCl buffer (1 M, pH 6.0) containing 0.2 mL of CPO (3, 000 U/mL) and stirred for 24 h at room temperature. The CPO enzyme was incorporated into the peptide nanogel network primarily through electrostatic interactions. The final ANCGs were recovered by centrifugation (9, 000 rpm), washed three times with deionized water, and the supernatant was retained to quantify residual CPO for calculating enzyme loading.

Determination of CPO loading and enzymatic activity
CPO encapsulation efficiency in ANCGs was calculated by subtracting the amount of residual enzyme (measured via UV absorbance at 403 nm) from the initial quantity added. Enzymatic activity of CPO was assessed through its standard catalytic conversion of monochlorodimedon (MCD) to dichlorodimedon (DCD) in the presence of KCl and H_2O_2. Specifically, either 29 μL of free CPO (3, 000 U/mL) or 140 μL of ANCGs (containing 87 U of CPO) was mixed with 0.1 M PBS (pH 2.75) supplemented with 0.1 mM MCD, 20 mM KCl, and 2 mM H_2O_2 to a final volume of 3 mL. The decrease in UV absorbance at 278 nm was monitored continuously at 25 °C, and the initial reaction rate within the first 30 s was used to evaluate CPO activity.

Material characterization
Transmission electron microscopy (TEM), scanning TEM (STEM), and energy-dispersive X-ray spectroscopy (EDS) images were acquired on a JEM 2100F microscope (JEOL Ltd., Tokyo, Japan) at an accelerating voltage of 200 kV. Particle size distributions for AuNRs and ANGs from TEM images were analyzed using ImageJ software. Hydrodynamic diameters and zeta potentials of the nanoparticles were measured with a Malvern Zetasizer Nano ZS90 instrument (Malvern, Worcestershire, UK). Thermogravimetric analysis (TGA) was performed on a Netzsch STA 409 analyzer (Netzsch, Hanau, Germany) under nitrogen flow, heating from room temperature to 900 °C at 10 °C/min. UV-visible absorption spectra were recorded on a Shimadzu UV-2700 spectrophotometer (Shimadzu, Kyoto, Japan). Electron paramagnetic resonance (EPR) spectra were obtained using a Bruker A300 spectrometer (Bruker Biospin, Billerica, MA, USA). Fourier transform infrared (FT-IR) spectra were collected on a FLUOROLOG-3-11 fluorophotometer (Horiba, Kyoto, Japan).

Evaluation of photothermal performance for ANGs and ANCGs

Aliquots (500 μL) of ANGs or ANCGs at varying concentrations (1.875, 3.75, 7.5, and 10 μg/mL) were placed in a quartz cuvette and irradiated with an 808 nm NIR laser (1.5 W/cm²; VLSM-808-B-004, Shanghai Baiantek Sensing Technology Co., Ltd., Shanghai, China) for ten min. Temperature elevations were recorded every 10 s using a thermocouple, with initial temperatures normalized to 24 ± 1 °C. Experiments were repeated three times, and results are presented as means ± standard deviation (SD) (n = 3).

In vitro assessment of singlet oxygen ($^1O_2$) generation

Singlet oxygen production by ANCGs was initially detected using EPR spectroscopy (JES FA200, Shanghai Aifei Electronic Technology Co., Ltd., Shanghai, China). A mixture comprising 200 μL of ANCGs (0.05 mM), 50 μL of NaCl (50 mM), 50 μL of H_2O_2 (500 mM), and TEMP (as a $^1O_2$ trap) was rapidly transferred to a quartz capillary, and EPR signals were recorded at 4-min intervals.

Additionally, $^1O_2$ formation was monitored via fluorescence using SOSG as a probe. A baseline mixture was prepared with 400 μL of NaCl (100 mM), 10 μL of H_2O_2 (10 mM), 40 μL of SOSG (0.1 mM), and 260 μL of deionized water in a cuvette. Then, 200 μL of ANCGs (0.05 mM) was added, and fluorescence emission spectra (excitation at 488 nm) were acquired at various time points.

Assessment of intracellular ROS production

To investigate intracellular ROS generation, SMMC-7721 human hepatocarcinoma cells were plated in six-well plates at a density of 1.0×10^5 cells per well and allowed to adhere for twenty four hours. The culture medium was then switched to serum-free medium for an additional 6 h incubation. Subsequently, cells were treated with PBS, ANGs, or ANCGs (Au concentration: 10 μg/mL) for 6 h. The medium was replaced with serum-free medium containing 10 μM DCFH-DA, and incubation continued for 1 h. For groups designated as NIR (+), cells received 808 nm laser irradiation (0.5 W/cm²) for ten minutes. Finally, cells were rinsed with PBS, and ROS-induced fluorescence was visualized using confocal laser scanning microscopy (CLSM) (excitation/emission: 488 nm/525 nm) on a Carl Zeiss system (Carl Zeiss AG, Jena, Germany).

Further quantification of cellular ROS levels was conducted via flow cytometry in both normal mouse embryonic fibroblasts (NIH-3T3) and SMMC-7721 cells using DCFH-DA as the probe. Both cell lines were seeded at 1.0×10^5 cells per well in six-well plates. For SMMC-7721 cells, the medium was replaced with serum-free medium, whereas NIH-3T3 cells remained in standard culture medium. After 6 h, cells were exposed to ANGs or ANCGs (Au concentration: 10 μg/mL) for another 6 h, with PBS serving as control. DCFH-DA (10 μM) was added, and cells were incubated for 20 min. NIR (+) groups underwent 808 nm laser exposure (0.5 W/cm²) for 10 min. Cells were then harvested by trypsinization and analyzed on a BD Accuri C6 flow cytometer (BD Accuri Cytometers Inc., Ann Arbor, MI, USA) (excitation/emission: 488 nm/525 nm).

In vitro cytotoxicity evaluation

The cytotoxic effects and biocompatibility of the nanoparticles were assessed using CCK-8 assays and live/dead staining. For CCK-8 assays, SMMC-7721 or NIH-3T3 cells were seeded at 5000 cells per well in 96-well plates and cultured for 24 h. The medium for SMMC-7721 cells was then changed to serum-free, while NIH-3T3 cells continued in normal medium. Various concentrations of ANGs or ANCGs (0, 1.875, 3.75, 7.5, and 10 μg/mL) were introduced. In NIR (+) groups, cells were irradiated with an 808 nm laser (0.5 W/cm²) for ten minutes after four hours of nanoparticle exposure, followed by 20 h further incubation; non-irradiated groups were cultured for a total of 24 h. CCK-8 reagent was added to each well for two hours , and absorbance at 450 nm was measured using a microplate reader (BioTek Instruments, Inc., Winooski, VT, USA).

For live/dead staining, SMMC-7721 cells were seeded at 1.0×10^5 cells per well in six-well plates, incubated for 24 h, and then switched to serum-free medium for 6 h. Cells were subsequently treated with PBS, ANGs, or ANCGs (Au concentration: 10 μg/mL) for 12 h. NIR (+) groups received 808 nm laser irradiation (0.5 W/cm²) for 10 min. Cells were stained with calcein-AM and propidium iodide for 30 min, washed with PBS, and imaged by CLSM.

Immunofluorescence staining for Nrf2 expression

To examine Nrf2 expression in tumor cells, SMMC-7721 cells cultured in six-well plates (1.0×10^5 cells per well) were treated for 6 h, washed three times with PBS, fixed in 4 percent paraformaldehyde, and permeabilized with

0.1 percent Triton X-100. Cells were incubated with primary anti-Nrf2 antibody (ab62352; Abcam, Cambridge, MA, USA) at 1:500 dilution, followed by Alexa Fluor® 488-conjugated goat anti-rabbit IgG secondary antibody (1:1000; A11008, Thermo Fisher Scientific Inc., Waltham, MA, USA). Nuclei were counterstained with 1 μg/mL DAPI (Beyotime Biotechnology). A negative control omitted the primary antibody and used PBS instead. After rinsing, fluorescence images were acquired using CLSM on an Olympus FV1000 system (Olympus America Inc., Center Valley, PA, USA).

In vivo antitumor efficacy studies

All animal procedures complied with the protocols approved by the Institutional Animal Care and Use Committee of Tongji University (Approval No.: TJAC00323106). An SMMC-7721 tumor xenograft model was established by subcutaneous injection of 1.5×10^6 cells into the right flank of 6–8-week-old nude mice. When tumors reached ~100 mm^3, mice were randomly assigned to groups (n = 4 per group) for either intratumoral or intravenous administration.

For intratumoral treatment, four groups received: 1) PBS (50 μL, pH 7.4); 2) ANGs (50 μL, 5 mg/mL) with NIR irradiation for ten minutes; 3) ANCGs (50 μL, 5 mg/mL); 4) ANCGs (50 μL, 5 mg/mL) with NIR irradiation for 10 min. Injections occurred on days zero, one, two, four, and seven, with immediate 808 nm laser irradiation (0.5 W/cm^2) post-injection where applicable.

For intravenous treatment, two additional groups received PBS (100 μL, pH 7.4) or ANCGs (100 μL, 5 mg/mL) on days zero, one, two, four, seven, eight, twelve, eighteen, and twenty four. Tumors in the ANCGs group were irradiated with 808 nm laser (0.5 W/cm^2) for 10 min at 24 h post-injection.

Tumor dimensions and body weights were monitored before each administration, with volumes calculated as $V = (\text{length} \times \text{width}^2)/2$. At study endpoint, mice were euthanized, and tumors plus major organs were harvested, sectioned, and subjected to hematoxylin and eosin (H&E) and TUNEL staining.

Statistical analysis

Data are presented as mean ± standard deviation (SD). Differences between groups were evaluated using Student's t-test. Statistical significance was defined as $^{**}P < 0.01$ and $^{***}P < 0.001$.

Results and Discussion

Synthesis and characterization of the ANCGs

Scheme 1 presents an illustration of the preparation pathway for enzyme-incorporated hybrid nanogel platforms, along with the processes underlying their combined photothermal-enzymatic treatment. Uniform-sized AuNRs were synthesized following an established protocol [39], after which their surface underwent carboxylation using HA-SH. The resulting AuNRs-COOH were initially activated with EDC/NHS, followed by conjugation of AP onto the AuNR surface to serve as catalytic seeds. Subsequently, the surface-bound AP catalyzed the removal of phosphate groups from the peptide precursor Fmoc-Tyr(H2PO3)-OH, generating a self-assembled hydrogel layer that encapsulated the gold nanorod cores and thereby forming the ANGs. In the final step, ANCGs were constructed through the incorporation of CPO into the ANGs, facilitated by electrostatic attraction between the hydrogel network and the enzyme. Within the tumor microenvironment, external near-infrared irradiation effectively elevates levels of intrinsic reactive oxygen species by inducing cellular stress through hyperthermia generated by the AuNR cores in the hybrid nanogels; this is followed by the generation of lethal singlet oxygen ($^1O_2$) via enzyme-catalyzed oxidation mediated by CPO in the nanogels, utilizing the elevated hydrogen peroxide (H_2O_2) present in cancerous tissues. Therefore, these ANCGs function as cascade-enhanced generators of both exogenous and endogenous ROS, enabling efficient and safe cancer treatment.

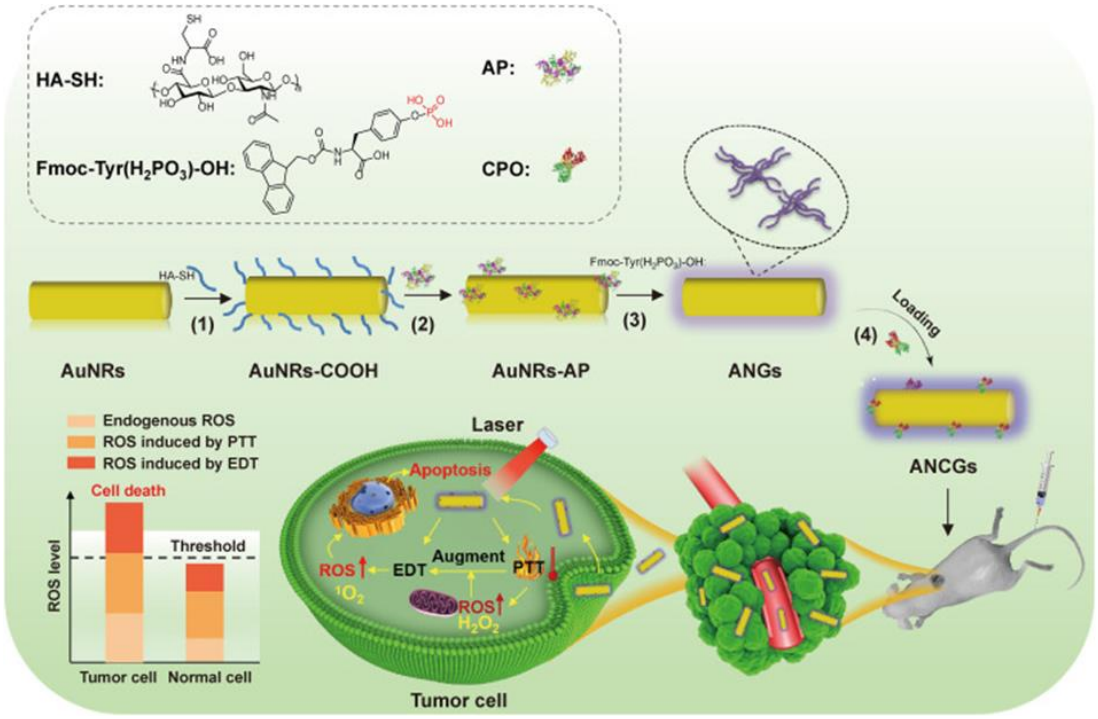

Scheme 1. Illustration depicting the fabrication process of gold nanorod (AuNR)-centered nanogels (ANGs) as well as the enzyme-incorporated hybrid nanogel platforms (ANCGs), together with the underlying mechanism of their combined photothermal-enzymatic therapeutic action. The steps involve: (1) introduction of carboxyl functionalities onto the AuNR surface through conjugation with thiolated hyaluronic acid (HA-SH), (2) activation of these carboxyl sites to enable covalent attachment of alkaline phosphatase (yielding AuNR-AP), (3) phosphatase-catalyzed removal of phosphate from the precursor N-(fluorenyl-methoxycarbonyl)-tyrosine phosphate (Fmoc-Tyr(H_2PO_3)-OH), followed by self-organization into a hydrogel shell to produce ANGs, and (4) incorporation of chloroperoxidase (CPO) within the ANGs through electrostatic binding. Tumor cells, unlike healthy cells, maintain elevated baseline reactive oxygen species (ROS) levels. In the tumor microenvironment, near-infrared (NIR) irradiation triggers the AuNR cores within the hybrid nanogels to significantly boost intrinsic ROS production via photothermal stress; this elevation then facilitates the CPO-mediated enzymatic oxidation to generate highly cytotoxic singlet oxygen ($^1O_2$). Consequently, the cascaded amplification of ROS surpasses critical thresholds, causing extensive damage to biomolecules and promoting tumor cell apoptosis. PTT: photothermal therapy; EDT: enzyme dynamic therapy.

The structural features and morphologies of the AuNRs and ANGs were examined by transmission electron microscopy (TEM), scanning transmission electron microscopy (STEM), and energy-dispersive X-ray spectroscopy (EDS). As displayed in **Figures 1a−1d**, the AuNRs showed consistent rod-shaped morphology with excellent dispersity and dimensions of roughly 45 nm in length by 15 nm in width, while the ANGs revealed a distinct core-shell architecture in dehydrated state, along with increased overall sizes of about 50 nm × 20 nm.

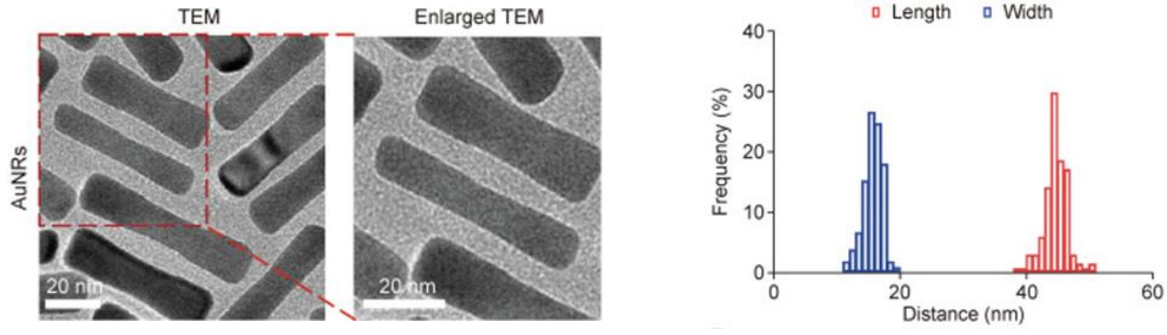

a) b)

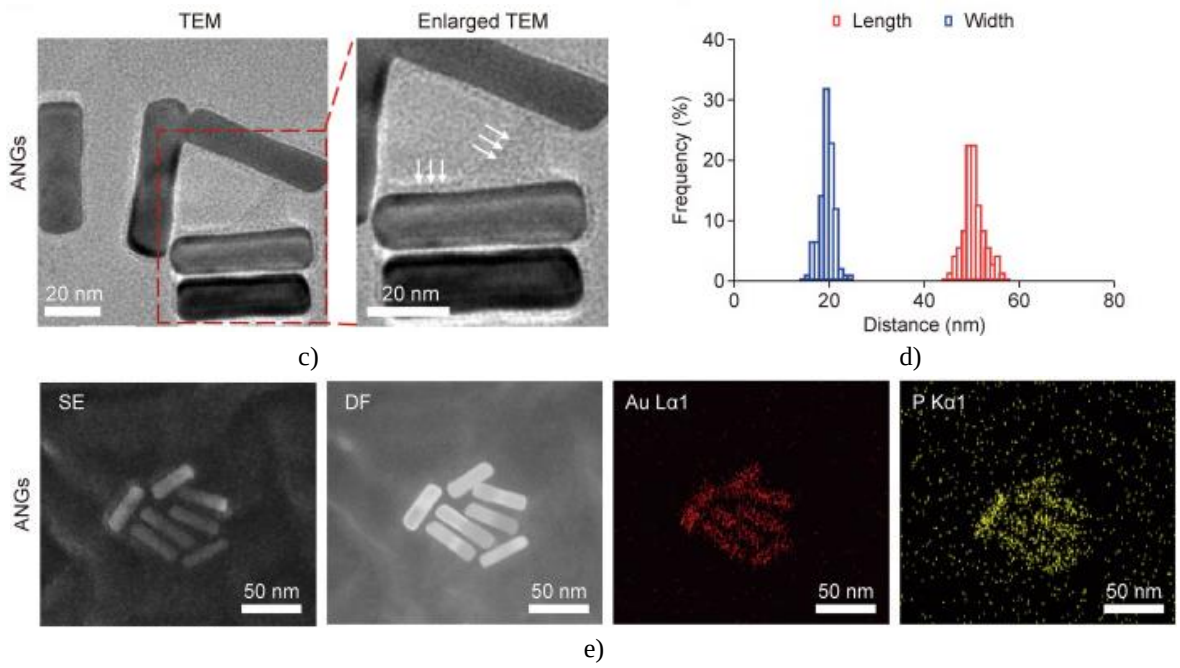

Figure 1. Structural and morphological characterization of gold nanorods (AuNRs) and AuNR-centered nanogels (ANGs). (a, b) Transmission electron microscopy (TEM) images of AuNRs along with their particle size distributions: TEM micrographs (a) and corresponding normalized size histograms (b). (c, d) TEM images of ANGs together with their particle size distributions: TEM micrographs (c) and normalized size histograms (d). Insets provide magnified views, where white arrows highlight the gel layer surrounding the AuNR surfaces. (e) Secondary electron (SE) image, dark-field (DF) image, and elemental mapping showing the spatial distribution of gold (Au) and phosphorus (P) in ANGs.

A distinct hydrogel shell with an average thickness of about 2 nm was readily visible around the AuNRs, confirming the effective formation of the hydrogel coating via the employed surface-initiated peptide self-assembly approach. The presence of these hydrogel nanoshells was further substantiated through STEM and EDS analyses, as illustrated in **Figure 1e**. STEM imaging of ANGs in both secondary electron (SE) and dark-field (DF) modes clearly revealed a pronounced core-shell architecture. Elemental distribution maps for ANGs displayed rod-shaped patterns for Au and phosphorus (P), providing additional evidence for the uniform hydrogel encapsulation of the AuNR cores.

Additionally, hydrodynamic size distributions for AuNRs and ANGs were determined by dynamic light scattering (DLS), as shown in **Figure 2a**. The mean hydrodynamic diameters were found to be 52 nm for AuNRs and 79 nm for ANGs, which further supports the successful deposition of the hydrogel layer. Zeta potential measurements, presented in **Figure 2b**, indicated a substantial drop from 13.1 mV to −18.7 mV upon carboxylation (AuNRs-COOH), followed by a rise to −11.3 mV for ANGs, thereby validating the carboxylation step and subsequent hydrogel shell formation. Thermogravimetric (TG) analysis in **Figure 2c** demonstrated a higher weight loss of 27.8% for dried ANGs relative to AuNRs, attributable to thermal decomposition of the organic hydrogel component. Furthermore, UV-vis spectroscopy was used to examine the surface plasmon resonance (SPR) properties of AuNRs and ANGs. As depicted in **Figure 2d**, AuNRs exhibited a longitudinal SPR peak at 810 nm, which red-shifted to 825 nm for ANGs due to the altered local refractive index induced by the surrounding hydrogel shell. Collectively, these findings affirm the successful synthesis of AuNR-based hybrid nanogels.

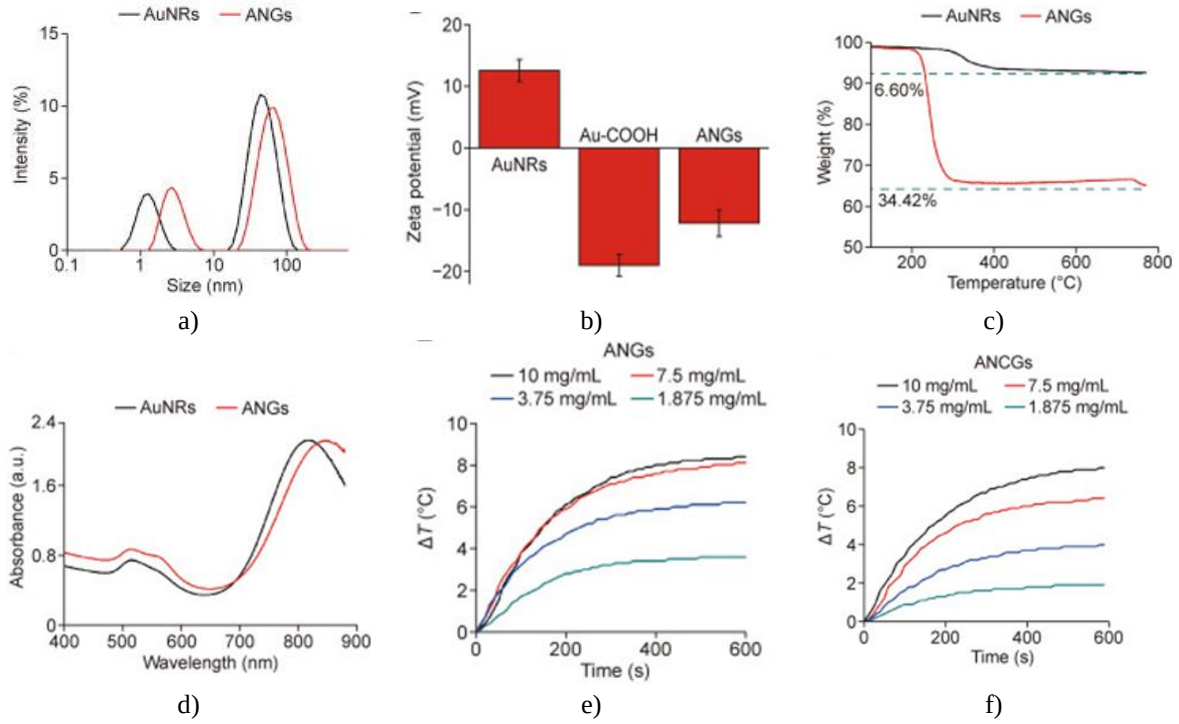

Figure 2. Further characterization of AuNR-centered nanogels (ANGs) and enzyme-incorporated hybrid nanogel platforms (ANCGs). (a) Hydrodynamic size distributions measured by dynamic light scattering (DLS) for AuNRs and ANGs. (b) Zeta potential values for pristine AuNRs, carboxylated AuNRs (AuNR–COOH), and ANGs. (c) Thermogravimetric (TG) analysis curves of AuNRs and ANGs. (d) UV-vis absorption spectra of the synthesized AuNRs and ANGs. (e, f) Photothermal heating profiles of ANGs (e) and ANCGs (f) under NIR irradiation.

The photothermal performance of the synthesized ANCGs was evaluated in vitro. In brief, aqueous dispersions of ANGs and ANCGs at varying gold concentrations (1.875, 3.75, 7.5, and 10 μg/mL) were exposed to an 808 nm near-infrared laser (1.5 W/cm²) for 10 min, while temperature elevations were recorded in real time every 10 s. The resulting temperature profiles are presented in **Figures 2e and 2f**. For both ANGs and ANCGs, solution temperatures rose markedly with irradiation duration, eventually stabilizing after 10 min. The extent of temperature increase was clearly dependent on Au concentration across the tested range (1.875–10 μg/mL). Specifically, at the highest Au concentration of 10 μg/mL, ANCGs achieved a temperature rise of 8.17 °C following 10 min of NIR exposure, which was nearly identical to that observed for ANGs (approximately 8.23 °C). These findings indicate that the ANCG hybrid nanogels exhibit outstanding photothermal conversion efficiency, and the incorporation of CPO exerts negligible influence on this property at elevated Au concentrations (10 μg/mL), highlighting their promise for subsequent in vivo photothermal applications.

In vitro $^1O_2$ generation

The ability to generate singlet oxygen ($^1O_2$) via enzymatic biocatalysis represents a critical element of the designed combined photothermal-enzymatic therapeutic strategy. Accordingly, the enzyme loading capacity and retained bioactivity of ANCGs were assessed, with results shown in **Figures 3a and 3b**. The CPO loading efficiency within ANCGs reached 52.5%, as quantified from the UV-vis absorbance peak at 398 nm. The catalytic activities of free CPO and CPO immobilized in ANCGs were compared using monochlorodimedone (MCD) as substrate, tracking the kinetic transformation of MCD to dichlorodimedone (DCD) by UV-vis spectroscopy. As depicted in **Figure 3a**, the immobilized CPO in ANCGs retained 81.7% of the initial reaction rate observed for free CPO. Furthermore, after incubation at 45 °C for 10 min, ANCGs preserved roughly 74.2% of their enzymatic activity **(Figure 3b)**, underscoring the robust catalytic performance of the fabricated ANCGs for effective substrate conversion.

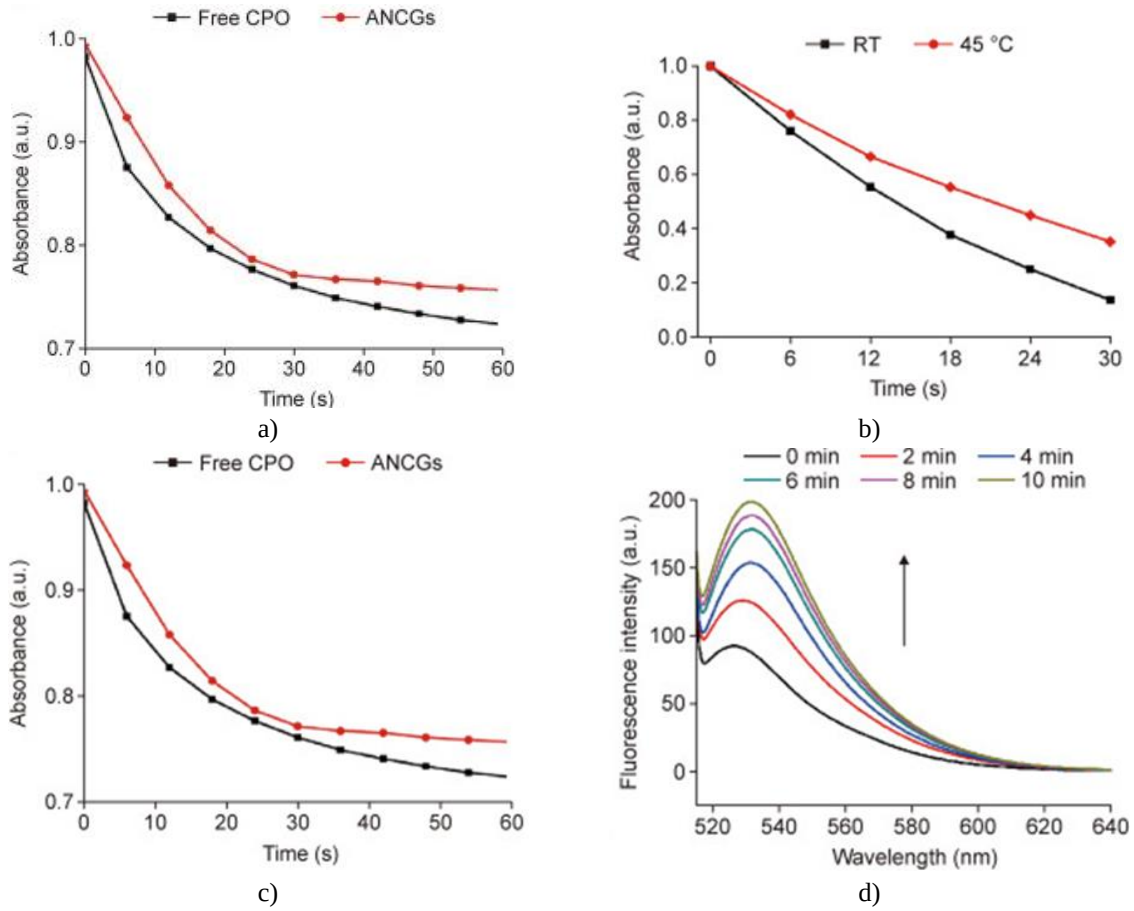

Figure 3. Evaluation of the in vitro enzymatic catalytic performance of AuNR-centered nanogels (ANGs) and enzyme-incorporated hybrid nanogel platforms (ANCGs). (a) Activity assessment of free chloroperoxidase (CPO) versus ANCGs in phosphate-buffered saline (PBS). (b) Comparative enzymatic activity of ANCGs at room temperature (RT, 25 °C) and at 45 °C. (c) Time-resolved electron paramagnetic resonance (EPR) spectra showing singlet oxygen ($^1O_2$) signals generated by ANCGs in NaCl solution supplemented with 100 μM H_2O_2, employing 2, 2, 6, 6-tetramethylpiperidine (TEMP) as the $^1O_2$ trap. (d) Time-dependent fluorescence spectra monitoring $^1O_2$ production by ANCGs in NaCl solution containing 100 μM H_2O_2, using singlet oxygen sensor green (SOSG) as the fluorescent indicator.

The generation of $^1O_2$ was further examined and confirmed via EPR under a mimicked endogenous condition (NaCl solution with 100 μM H_2O_2), utilizing TEMP as the $^1O_2$ scavenger. As presented in **Figure 3c**, the EPR spectra displayed a characteristic 1:1:1 triplet signal indicative of $^1O_2$, with signal intensity progressively strengthening as the measurement duration extended from 0 to 16 min. Complementary fluorescence measurements were conducted to track $^1O_2$ formation, employing SOSG as the probe. The time-course fluorescence spectra for the ANCGs-catalyzed oxidation of Cl^- by H_2O_2 are shown in **Figure 3d**. Consistent with expectations, fluorescence intensity steadily rose over the reaction period from 0 to 10 min, aligning well with the EPR observations and demonstrating a continuous $^1O_2$ production during the enzymatic process. Moreover, the robust bioactivity retained by ANCGs ensures superior efficiency in $^1O_2$ generation. These collective data verify that the developed ANCGs are capable of effectively promoting sustained $^1O_2$ formation within a simulated endogenous setting.

Enhancement of oxidative stress through intracellular ROS generation via photothermal-enzymatic synergy

In line with the designed photothermal-enzymatic synergistic mechanism, near-infrared irradiation can boost endogenous ROS levels in cancer cells—including H_2O_2—which in turn drives CPO-mediated enzymatic production of $^1O_2$, thereby further escalating intracellular ROS to therapeutic levels. To validate this concept, changes in cellular ROS concentrations triggered by the combined photothermal-enzymatic action of ANCGs were explored in SMMC-7721 cells. Following a 4 h co-incubation of SMMC-7721 cells with PBS, ANGs, or

ANCGs, and subsequent exposure (or no exposure) to an 808 nm NIR laser for 10 min, the ROS-sensitive probe DCFH-DA was introduced to assess intracellular ROS via confocal laser scanning microscopy (CLSM). As illustrated in **Figure 4a**, cells treated with ANCGs (without NIR) displayed noticeable green fluorescence relative to the ANGs group, indicating intracellular $^1O_2$ production arising from the enzymatic activity. Furthermore, NIR-irradiated cells pretreated with ANGs (ANGs/NIR) exhibited marked fluorescence intensification. Notably, the ANCGs/NIR treatment group produced substantially brighter green ROS signals compared to both the standalone ANCGs and ANGs/NIR groups, which can be ascribed to the cooperative photothermal-enzymatic effects of the ANCGs.

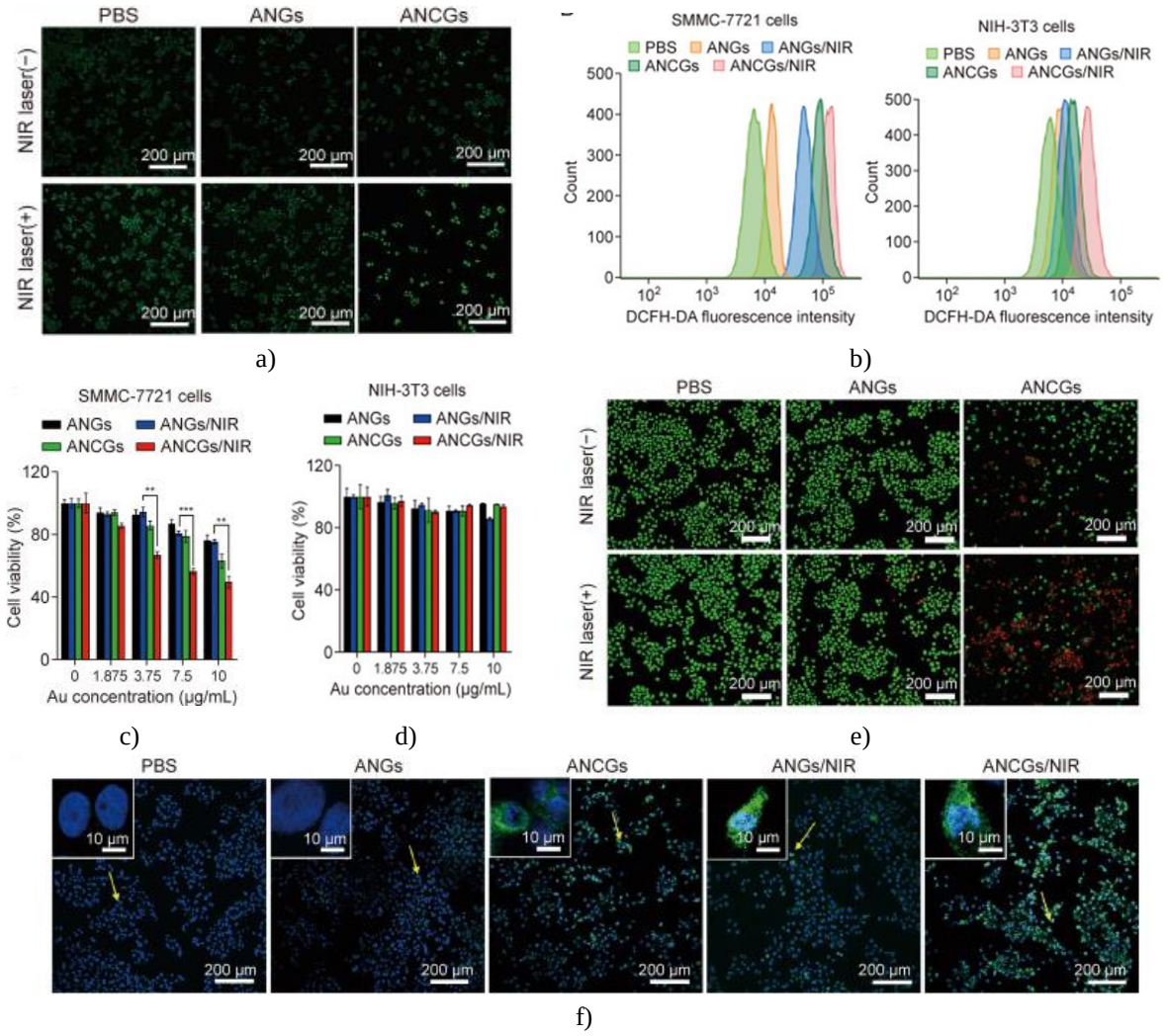

Figure 4. Intracellular assessment of combined enzyme dynamic therapy (EDT) and photothermal therapy (PTT). (a) Representative confocal fluorescence images depicting reactive oxygen species (ROS) production in human hepatocellular carcinoma (SMMC-7721) cells under various treatment conditions. (b) Flow cytometry analysis of ROS levels in SMMC-7721 cells and normal mouse embryonic fibroblasts (NIH-3T3) following different treatments. (c, d) Cell viability of SMMC-7721 (c) and NIH-3T3 (d) cells after incubation with varying concentrations of AuNR-centered nanogels (ANGs) and enzyme-incorporated hybrid nanogel platforms (ANCGs), with or without laser irradiation. Data are expressed as mean ± standard deviation (SD) (n = 5). $^{**}P < 0.01$ and $^{***}P < 0.001$. (e) Live/dead staining images of SMMC-7721 cells subjected to different treatments. (f) Expression and nuclear translocation of nuclear factor erythroid 2-related factor 2 (Nrf2) in SMMC-7721 cells after various treatments. Yellow arrows highlight enlarged representative cells. PBS: phosphate-buffered saline; NIR: near-infrared; DCFH-DA: 2′, 7′-dichlorodihydrofluorescein diacetate.

Flow cytometry was further employed to quantify ROS production in both NIH-3T3 and SMMC-7721 cells following treatment with PBS, ANGs, or ANCGs, with or without NIR irradiation. As shown in **Figure 4b**, normal

NIH-3T3 cells displayed only minor elevations in endogenous ROS even after ANCGs/NIR exposure, indicating that ROS generation in healthy cells remains insufficient to exceed the redox threshold for cytotoxicity, owing to their robust antioxidant mechanisms. In marked contrast, SMMC-7721 cells subjected to ANCGs/NIR exhibited substantially higher fluorescence intensities than all other groups (PBS, ANGs, ANGs/NIR, and ANCGs alone), underscoring the superior ROS-enhancing capability of the proposed photothermal-enzymatic cooperative approach. These findings align closely with the CLSM-based ROS detection and validate the multilevel ROS amplification enabled by the photothermal-enzymatic synergy of ANCGs, highlighting their therapeutic potential for cancer.

In vitro cytotoxicity assessment

The cytotoxic effects of ANGs and ANCGs on SMMC-7721 cancer cells and NIH-3T3 normal cells were examined via CCK-8 assays to assess the effectiveness and biosafety of the photothermal-enzymatic synergistic strategy. As illustrated in **Figure 4c**, ANGs under NIR irradiation exerted minimal influence on SMMC-7721 cell proliferation, while ANCGs without irradiation similarly showed limited cytotoxicity, reflecting inadequate ROS production from isolated photothermal or enzymatic oxidation modalities in tumor cells. However, upon NIR exposure, ANCGs markedly suppressed proliferation in SMMC-7721 cells, reducing viability to 49% at 10 μg/mL, in agreement with the mechanism whereby NIR-triggered ROS elevation activates CPO to amplify $^1O_2$ production and induce cancer cell death. The biocompatibility of the hybrid nanogels was further evaluated in NIH-3T3 cells across concentrations from 1.875 to 10 μg/mL, with or without NIR. As displayed in **Figure 4d**, neither ANGs nor ANCGs caused significant viability loss in normal cells regardless of irradiation, with survival rates exceeding 90% even at the highest concentration (10 μg/mL), confirming the low toxicity and excellent safety profile of this nanotherapeutic platform toward healthy tissues.

Live/dead staining assays were also conducted to visualize treatment-induced cytotoxicity in SMMC-7721 cells. Following calcein-AM/PI staining, confocal images **(Figure 4e)** revealed sparse red-fluorescent dead cells in the ANCGs and ANGs/NIR groups compared to controls, with predominant green live-cell signals persisting. In sharp contrast, ANCGs combined with NIR irradiation led to a dramatic rise in red-fluorescent cells, evidencing the most potent therapeutic outcome. These observations corroborate the CCK-8 results, showing that standalone photothermal or enzymatic effects deliver sublethal ROS doses, whereas the combined photothermal-enzymatic synergy achieves markedly superior antitumor efficacy through cascaded ROS escalation.

Immune response triggered by intracellular ROS accumulation

Under mild oxidative stress, the Nrf2 pathway is engaged to counteract hyperoxidation or hyperthermia, thereby supporting cell survival. However, when ROS exceeds a critical threshold, Nrf2 expression surges and translocates to the nucleus, paradoxically intensifying oxidative damage and promoting cell death [40]. Nrf2 expression was upregulated in SMMC-7721 cells treated with H_2O_2 or ANCGs, with fluorescence intensifying dose-dependently for both H_2O_2 and ANCGs/NIR, verifying pathway activation by elevated oxidation. Nrf2 responses to photothermal-enzymatic synergy were then examined. As depicted in **Figure 4f**, ANCGs, ANGs/NIR, and especially ANCGs/NIR treatments elicited pronounced Nrf2 upregulation and nuclear accumulation relative to PBS and ANGs controls, consistent with intracellular ROS induction via PTT and EDT. The ANCGs/NIR group displayed the strongest fluorescence, attributable to the amplified photothermal-enzymatic action. These data demonstrate that ANCGs/NIR effectively generates excessive ROS, driving Nrf2 expression and nuclear shuttling, which ultimately contributes to cancer cell demise.

In vivo antitumor efficacy and biosafety assessment

Building on promising in vitro results, the photothermal-enzymatic synergistic performance was evaluated in vivo using SMMC-7721 tumor-bearing nude mice. Animals with tumors of 80–100 mm^3 were randomly assigned to four groups: PBS, ANGs/NIR, ANCGs, and ANCGs/NIR. For irradiated groups, intratumoral injections were followed by 10 min of 808 nm NIR exposure (0.5 W/cm^2) **(Figure 5a)**. Tumors in the ANCGs/NIR group underwent evident regression, with relative volumes dropping to approximately 1.0 after seven days, reflecting superior therapeutic outcome from synergy-driven ROS amplification within the tumor site **(Figure 5b)**. Conversely, PBS, ANGs/NIR, and ANCGs groups displayed rapid tumor progression. Relative to PBS, ANGs/NIR and ANCGs exerted moderate growth inhibition, ascribable to isolated PTT or enzymatic contributions. Throughout the seven-day monitoring, all groups maintained stable body weight gains **(Figure 5c)**,

indicating negligible systemic toxicity and confirming the biosafety of the developed ANCGs as a photothermal-enzymatic synergistic agent.

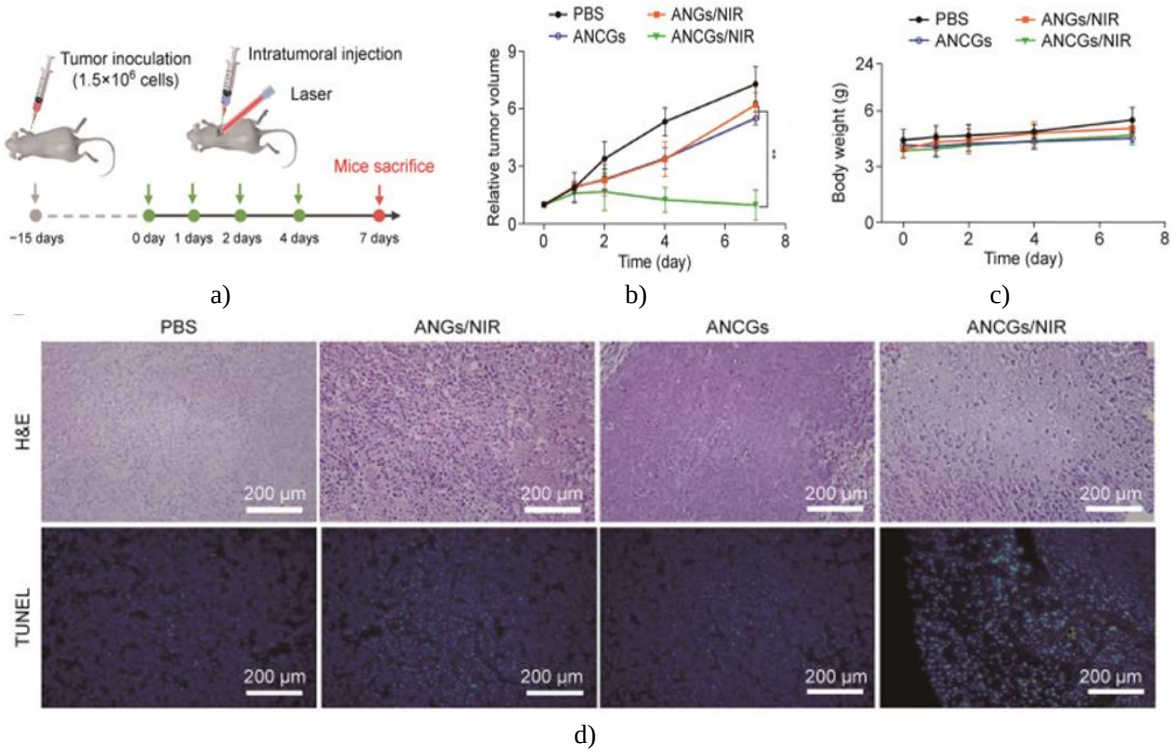

Figure 5. In vivo evaluation of the therapeutic performance of AuNR-centered nanogels (ANGs) and enzyme-incorporated hybrid nanogel platforms (ANCGs) following intratumoral administration. (A) Illustration of the treatment protocol in tumor-bearing nude mice via intratumoral injection. (B, C) Curves depicting relative tumor volume changes (B) and body weight variations (C) over seven days post-treatment. Data are shown as mean ± standard deviation (SD) (n = 4). ∗∗P < 0.01. (D) Hematoxylin and eosin (H&E) staining and terminal deoxynucleotidyl transferase dUTP nick-end labeling (TUNEL) images of tumor sections collected seven days after the respective treatments. PBS: phosphate-buffered saline; NIR: near-infrared.

Seven days post-treatment, the mice were euthanized, and tumors along with major organs were harvested for histopathological examination. Tumor tissue damage and apoptosis were assessed in detail through H&E and TUNEL staining. As displayed in **Figure 5d**, tumor sections from the ANGs/NIR and ANCGs groups exhibited varying degrees of cellular injury and apoptotic signals in both H&E and TUNEL images, attributable to the standalone effects of NIR-induced photothermal stress and CPO-driven ROS elevation, respectively, which aligns with the in vitro cytotoxicity findings. Strikingly, the ANCGs/NIR group demonstrated the most extensive tissue destruction and apoptosis, underscoring the superior therapeutic efficacy of ANCGs when combined with NIR irradiation.

Furthermore, the SMMC-7721 tumor-bearing mouse model was subjected to intravenous administration **(Figure 6a)**. Consistent with the intratumoral injection outcomes, the ANCGs/NIR group achieved pronounced tumor growth suppression, while body weights remained stable throughout the 24-day observation period **(Figures 6b and 6c)**. H&E and TUNEL staining of tumor sections confirmed that ANCGs/NIR treatment induced severe histological damage and widespread apoptosis within the tumors **(Figure 6d)**. Simultaneously, major organs were retrieved and sectioned for analysis. H&E-stained images of the heart, liver, spleen, lung, and kidney revealed no discernible pathological changes or inflammatory responses, affirming the excellent biosafety of ANCGs toward healthy tissues **(Figure 6e)**. Collectively, the results from both intratumoral and intravenous administration validate the proposed photothermal-enzymatic synergistic ROS-amplification approach as a highly effective and safe modality for cancer treatment.

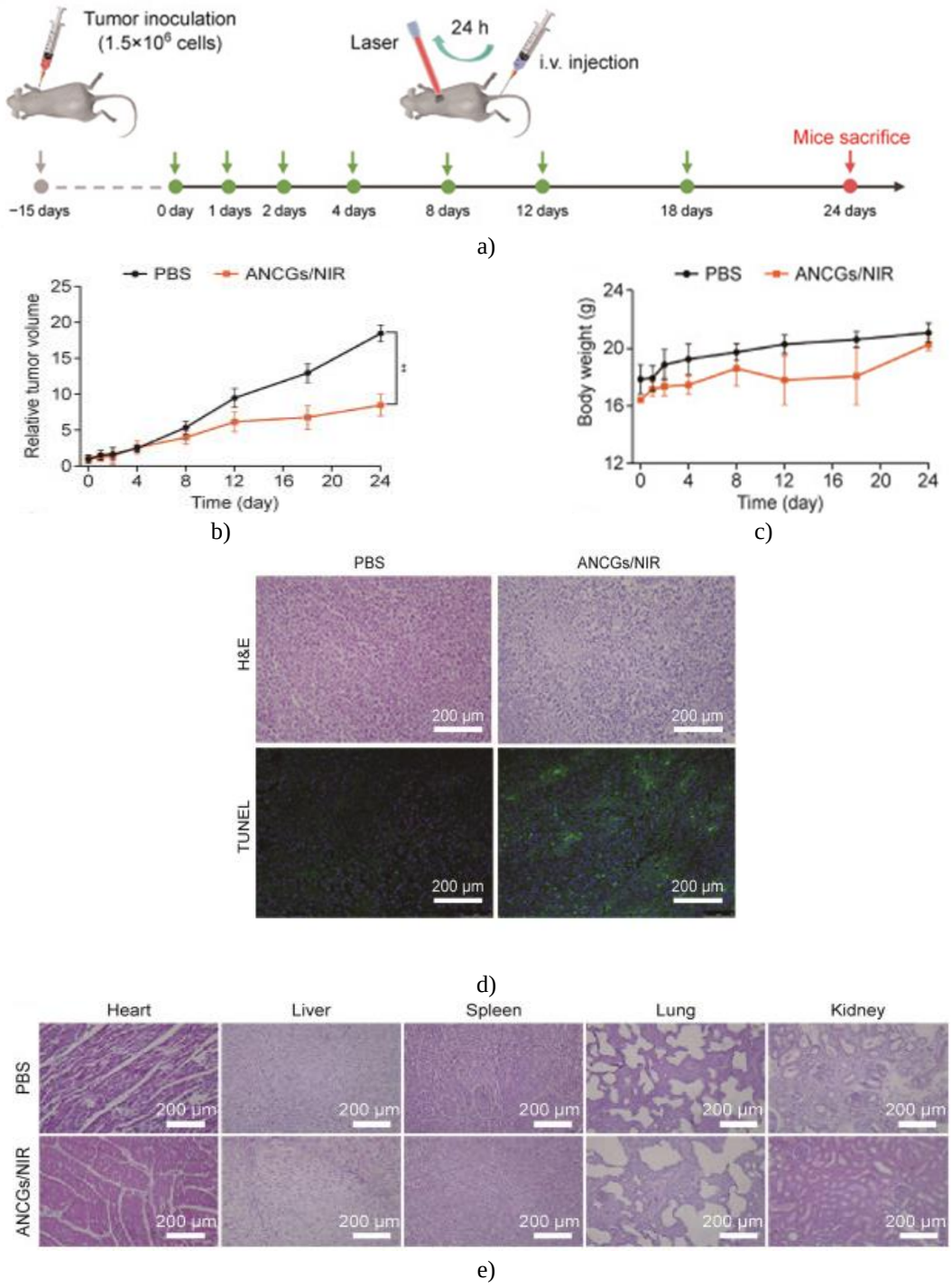

Figure 6. Assessment of antitumor efficacy of AuNR-centered nanogels (ANGs) and enzyme-incorporated hybrid nanogel platforms (ANCGs) in SMMC-7721 tumor-bearing mice. (a) Illustration of the in vivo treatment protocol in tumor-bearing nude mice via intravenous (i.v.) administration. (b, c) Curves showing relative tumor volume changes (b) and body weight variations (c) over 24 days following different treatments. Data are expressed as mean ± standard deviation (SD) (n = 4). $**P < 0.01$. (d) Hematoxylin and eosin (H&E) and terminal deoxynucleotidyl transferase dUTP nick-end labeling (TUNEL) staining images of tumor sections after 24 days of treatment. (e) H&E staining images of major organs harvested from mice after 24 days of treatment. PBS: phosphate-buffered saline; NIR: near-infrared.

Conclusion

In summary, we have successfully developed a potent photothermal-enzymatic synergistic platform for multilevel ROS-enhanced cancer therapy, based on AuNR-centered hybrid nanogels loaded with CPO. Upon 808 nm laser

irradiation, ANCGs induce intracellular ROS production through photothermal heating, while the elevated ROS (particularly H_2O_2) concurrently drives sustained enzymatic generation of $^1O_2$, leading to cascade-amplified ROS levels that exceed the cellular antioxidant threshold and trigger tumor cell apoptosis, leaving healthy cells unharmed. The synergistic photothermal-enzymatic action, along with excellent biosafety, was substantiated through in vitro cytotoxicity evaluations and in vivo antitumor studies. This work presents a promising strategy for exogenous/endogenous cascade-amplified ROS generation in safe and efficient cancer treatment, combining spatiotemporally precise physical triggering with intrinsic biochemical oxidation, and provides significant inspiration for advancing synergistic ROS-based therapeutic modalities.

Acknowledgments: None

Conflict of Interest: None

Financial Support: None

Ethics Statement: None

References

1. Hanahan D, Weinberg RA. Hallmarks of cancer: the next generation. Cell. 2011;144(5):646-74.
2. Cairns RA, Harris IS, Mak TW. Regulation of cancer cell metabolism. Nat Rev Cancer. 2011;11(2):85-95.
3. Gorrini C, Harris IS, Mak TW. Modulation of oxidative stress as an anti-cancer strategy. Nat Rev Drug Discov. 2013;12(12):931-47.
4. Schieber M, Chandel NS. ROS function in redox signaling and oxidative stress. Curr Biol. 2014;24(10):R453-62.
5. He L, Chen J, Deng P, Zhang X, Wang Y, Li H, et al. Lysosomal cyst(e)ine storage potentiates tolerance to oxidative stress in cancer cells. Mol Cell. 2023;83(19):3502-19.e11.
6. Prasad S, Gupta SC, Tyagi AK. Reactive oxygen species (ROS) and cancer: role of antioxidative nutraceuticals. Cancer Lett. 2017;387:95-105.
7. Somu P, Mohanty S, Paul S. A detailed overview of ROS-modulating approaches in cancer treatment: nano-based system to improve its future clinical perspective. In: Chakraborti S, editor. Handbook of Oxidative Stress in Cancer: Therapeutic Aspects. Singapore: Springer; 2021. p. 1-22.
8. Yang B, Chen Y, Shi J. Reactive oxygen species (ROS)-based nanomedicine. Chem Rev. 2019;119(8):4881-985.
9. Raj L, Ide T, Gurkar AU, Foley M, Schenone M, Li X, et al. Selective killing of cancer cells by a small molecule targeting the stress response to ROS. Nature. 2011;475(7355):231-4.
10. Trachootham D, Alexandre J, Huang P. Targeting cancer cells by ROS-mediated mechanisms: a radical therapeutic approach? Nat Rev Drug Discov. 2009;8(7):579-91.
11. Zhang C, Wang X, Du J, Gu Z, Zhao Y. Reactive oxygen species-regulating strategies based on nanomaterials for disease treatment. Adv Sci (Weinh). 2021;8(3):2002797.
12. Zhou Z, Song J, Nie L, Chen X. Reactive oxygen species generating systems meeting challenges of photodynamic cancer therapy. Chem Soc Rev. 2016;45(23):6597-626.
13. Kwon S, Ko H, You DG, Kataoka K, Park JH. Nanomedicines for reactive oxygen species mediated approach: an emerging paradigm for cancer treatment. Acc Chem Res. 2019;52(7):1771-82.
14. Cheng Y, Cheng H, Jiang C, Qiu X, Wang K, Huan W, et al. Perfluorocarbon nanoparticles enhance reactive oxygen levels and tumour growth inhibition in photodynamic therapy. Nat Commun. 2015;6:8785.
15. Liu Y, Liu Y, Bu W, Cheng C, Zuo C, Xiao Q, et al. Hypoxia induced by upconversion-based photodynamic therapy: towards highly effective synergistic bioreductive therapy in tumors. Angew Chem Int Ed Engl. 2015;54(28):8105-9.
16. Li WP, Su CH, Chang YC, Lin YJ, Yeh CS. Ultrasound-induced reactive oxygen species mediated therapy and imaging using a Fenton reaction activable polymersome. ACS Nano. 2016;10(2):2017-27.
17. Zhang Y, Zhang X, Yang H, Yu L, Xu Y, Sharma A, et al. Advanced biotechnology-assisted precise sonodynamic therapy. Chem Soc Rev. 2021;50(19):11227-48.

18. Li J, Luo Y, Pu K. Electromagnetic nanomedicines for combinational cancer immunotherapy. Angew Chem Int Ed Engl. 2021;60(23):12682-705.
19. Li J, Luo Y, Zeng Z, Merkle CW, Chen L, Meng X, et al. Precision cancer sono-immunotherapy using deep-tissue activatable semiconducting polymer immunomodulatory nanoparticles. Nat Commun. 2022;13(1):4032.
20. Li J, Yu N, Cui D, Ren X, Zhang Y, Wang H, et al. Activatable semiconducting polymer pro-nano-modulators for deep-tissue sono-immunotherapy of orthotopic pancreatic cancer. Angew Chem Int Ed Engl. 2023;62(33):e202305200.
21. Tang Z, Liu Y, He M, Bu W. Chemodynamic therapy: tumour microenvironment-mediated Fenton and Fenton-like reactions. Angew Chem Int Ed Engl. 2019;58(4):946-56.
22. Lin H, Chen Y, Shi J. Nanoparticle-triggered in situ catalytic chemical reactions for tumour-specific therapy. Chem Soc Rev. 2018;47(6):1938-58.
23. Qin X, Wu C, Niu D, Qin L, Wang X, Wang Q, et al. Peroxisome inspired hybrid enzyme nanogels for chemodynamic and photodynamic therapy. Nat Commun. 2021;12(1):5243.
24. Wu Q, He Z, Wang X, Zhang Q, Wei Q, Ma H, et al. Cascade enzymes within self-assembled hybrid nanogel mimicked neutrophil lysosomes for singlet oxygen elevated cancer therapy. Nat Commun. 2019;10(1):240.
25. Zhang Q, Wu J, Wang J, Liu Y, Ren J, Qu X. A neutrophil-inspired supramolecular nanogel for magnetocaloric-enzymatic tandem therapy. Angew Chem Int Ed Engl. 2020;59(10):3732-8.
26. Wu C, Qin L, Niu D, Wang X, Wang Q, Li Y, et al. A compartmental silica nanoreactor for multienzyme-regulated superactive catalytic therapy. Adv Funct Mater. 2021;31(31):2103531.
27. Yang M, Zhu M, Chen Y, Zhang Y, Liu J, Wang H. FePS3 nanosheets: preparation and potential in photothermal-photodynamic therapy. J Inorg Mater. 2021;36(10):1074-82.
28. Liu Y, Bhattarai P, Dai Z, Chen X. Photothermal therapy and photoacoustic imaging via nanotheranostics in fighting cancer. Chem Soc Rev. 2019;48(7):2053-108.
29. Gao G, Jiang Y, Guo Y, Jia H, Sun W, Zhao X, et al. Enzyme-mediated tumor starvation and phototherapy enhance mild-temperature photothermal therapy. Adv Funct Mater. 2020;30(16):1909391.
30. Sun H, Yu T, Li X, Xu J, Zhang Y, Wang J, et al. Second near-infrared photothermal-amplified immunotherapy using photoactivatable composite nanostimulators. J Nanobiotechnology. 2021;19(1):433.
31. Li X, Sun H, Li H, Hu C, Luo Y, Shi X, et al. Multi-responsive biodegradable cationic nanogels for highly efficient treatment of tumors. Adv Funct Mater. 2021;31(22):2100227.
32. An D, Fu J, Zhang B, Xie S, Shi H, Cheng D, et al. NIR-II responsive inorganic 2D nanomaterials for cancer photothermal therapy: recent advances and future challenges. Adv Funct Mater. 2021;31(30):2101625.
33. Gao L, Liu R, Gao F, Wang Y, Jiang X, Gao X. Plasmon-mediated generation of reactive oxygen species from near-infrared light excited gold nanocages for photodynamic therapy in vitro. ACS Nano. 2014;8(7):7260-71.
34. Kuo WS, Chang CN, Chang YT, Yang MH, Chien YH, Chen SJ, et al. Gold nanorods in photodynamic therapy, as hyperthermia agents, and in near-infrared optical imaging. Angew Chem Int Ed Engl. 2010;49(15):2711-5.
35. Gao D, Shi Y, Ni J, Li H, Chen X, Wang Z, et al. NIR/MRI-guided oxygen-independent carrier-free anti-tumor nano-theranostics. Small. 2022;18(8):e2106000.
36. Jia J, Liu G, Xu W, Tian X, Chen L, Han Y, et al. Fine-tuning the homometallic interface of Au-on-Au nanorods and their photothermal therapy in the NIR-II window. Angew Chem Int Ed Engl. 2020;59(34):14443-8.
37. Jang B, Park JY, Tung CH, Kim IH, Choi Y. Gold nanorod-photosensitizer complex for near-infrared fluorescence imaging and photodynamic/photothermal therapy in vivo. ACS Nano. 2011;5(2):1086-94.
38. Kanofsky JR. Singlet oxygen production by chloroperoxidase-hydrogen peroxide-halide systems. J Biol Chem. 1984;259(9):5596-600.
39. Zhang Z, Wang L, Wang J, Jiang X, Li X, Hu Z, et al. Mesoporous silica-coated gold nanorods as a light-mediated multifunctional theranostic platform for cancer treatment. Adv Mater. 2022;34(42):e2205637.
40. Zucker SN, Fink EE, Bagati A, Mannava S, Bianchi-Smiraglia A, Bogner PN, et al. Nrf2 amplifies oxidative stress via induction of Klf9. Mol Cell. 2014;53(6):916-28.